2D Materials

Dielectric breakdown and sub-wavelength patterning of monolayer hexagonal boron nitride using femtosecond pulses

To cite this article: Sabeeh Irfan Ahmad *et al* 2023 *2D Mater.* **10** 045029

IOP Publishing 2D Mater. 10 (2023) 045029 https://doi.org/10.1088/2053-1583/acfa0f

2D Materials

OPEN ACCESS

RECEIVED
26 April 2023

REVISED
23 August 2023

ACCEPTED FOR PUBLICATION
14 September 2023

PUBLISHED
25 September 2023

PAPER

Dielectric breakdown and sub-wavelength patterning of monolayer hexagonal boron nitride using femtosecond pulses

Sabeeh Irfan Ahmad[1], **Arpit Dave**[1], **Emmanuel Sarpong**[1], **Hsin-Yu Yao**[2], **Joel M Solomon**[1], **Jing-Kai Jiang**[3], **Chih-Wei Luo**[3], **Wen-Hao Chang**[3,4] **and Tsing-Hua Her**[1,*]

[1] Department of Physics and Optical Science, The University of North Carolina at Charlotte, 9201 University City Boulevard, Charlotte, NC 28223, United States of America
[2] Department of Physics, National Chung Cheng University, No.168, Sec. 1, University Rd., Minhsiung, Chiayi 621301, Taiwan
[3] Department of Electrophysics, National Yang Ming Chiao Tung University, Hsinchu 30010, Taiwan
[4] Research Center for Applied Sciences, Academia Sinica, Taipei 11529, Taiwan
[*] Author to whom any correspondence should be addressed.

E-mail: ther@uncc.edu

Keywords: materials processing, ultrafast processes in condensed matter, including semiconductors, nonlinear optics, nonlinear materials, hexagonal boron nitride

Supplementary material for this article is available online

Abstract

Hexagonal boron nitride (hBN) has emerged as a promising two-dimensional (2D) material for many applications in electronics and photonics. Although its linear and nonlinear optical properties have been extensively studied, the interaction of hBN with high-intensity laser pulses, which is important for realizing high-harmonic generation, creating deterministic defects as quantum emitters, and resist-free patterning in this material, has not been investigated. Here we report the first systematic study of dielectric breakdown in chemical vapor deposition (CVD)-grown hBN monolayers induced by single femtosecond laser pulses. We report a breakdown fluence of 0.7 J cm^{-2}, which is at least 7× higher than that of other monolayer 2D materials. A clean removal of hBN without leaving traces behind or causing lateral damage is demonstrated. The ablation features exhibit excellent fidelity with very small edge roughness, which we attribute to its ultrahigh fracture toughness due to its heterogeneous nature with three-fold symmetry. Moreover, even though defects are known to be abundant in CVD-grown hBN, we show experimentally and theoretically that its nonlinear optical breakdown is nearly intrinsic as defects only marginally lower the breakdown threshold. On top of this, we observe that hBN monolayers have a 4–5× lower breakdown threshold than their bulk equivalent. The last two observations can be understood if the carrier generation in monolayers is intrinsically enhanced due to its 2D nature. Finally, we demonstrate laser patterning of array of holes and lines in hBN with sub-wavelength feature sizes. Our work advances the fundamental knowledge of light-hBN interaction in the strong field regime and firmly establishes femtosecond lasers as novel and promising tools for resist-free patterning of hBN monolayers with high fidelity.

1. Introduction

Hexagonal boron nitride (hBN) has emerged as a promising two-dimensional (2D) material for many applications in electronics and photonics due to its large bandgap, mechanical flexibility and breaking strength, high thermal conductivity [1], and chemical stability [2]. Its linear [3] and nonlinear optical properties in the weak limit [4, 5] have been extensively studied. To date, little is known about hBN's response to the strong fields in high-intensity laser pulses. Such knowledge is very useful for many applications. For example, high-harmonic generation in hBN has been theoretically predicted but not yet demonstrated experimentally [6]. Knowledge of material degradation and optical breakdown thresholds induced by high-intensity ultrashort pulses would be particularly useful for this future work. As another example, spin defects in hBN have been extensively studied as quantum emitters due to their brightness and spin-dependent emission at room temperature [7]. Engineering deterministic defects in hBN induced by femtosecond laser pulses has been actively pursued, revealing that spin defects were only found around the edge of ablated features [7, 8]. Understanding the physics of optical breakdown in hBN therefore constitutes the first step towards engineering these defects in hBN. Furthermore, there has been a growing interest in laser patterning of 2D materials. Compared to photo/e-beam lithography and ion/e-beam direct etching, laser direct writing avoids the use of resists [9], eliminates unintentional damage from backscattered electrons [10], forgoes the need of high vacuum [11], and is a high-speed technique for prototyping. Many groups have demonstrated fabrication of holes and grooves in low-bandgap 2D materials (including graphene, MoS_2, and $PtSe_2$) using short-pulsed lasers with sub-wavelength resolution (∼100 nm) [12, 13] and high speed (50 mm s^{-1}) [14]. Similar features, if can be realized in hBN, can enable many important applications, such as metasurfaces (hole arrays and gratings) for mid-infrared polaritonic optical sensing [15], waveguides and micro-resonators [16], and patterning gate insulators and passivation layers. Moreover, using pulse energy right below the breakdown threshold may create controlled defects to fine tune tunneling barriers for 2D electronics. To date, although femtosecond laser ablation of hBN has been reported [7, 8], the physics of optical breakdown is not known and laser patterning of hBN has not been demonstrated.

Here, we report the first systematic study of optical breakdown of hBN monolayers induced by a single femtosecond laser pulse. We demonstrate that hBN has the highest breakdown threshold among all 2D materials, and femtosecond ablation removes hBN without leaving traces behind or causing lateral damage. The ablation features exhibit excellent fidelity which we attribute to its heterogeneous nature with three-fold symmetry. Moreover, even though defects are known to be abundant in chemical vapor deposition (CVD)-grown hBN, we prove experimentally and theoretically that its nonlinear optical breakdown is nearly intrinsic, i.e. defects only marginally lower the breakdown threshold. Combined this with the additional observation that monolayers have a 4–5× smaller breakdown threshold than their bulk equivalent, we conclude that carrier generation in monolayers is enhanced. Finally, we demonstrate rudimentary laser patterning of hBN with sub-wavelength feature sizes. Our work clearly positions femtosecond laser ablation as a promising tool for resist-free patterning of hBN.

2. Materials and methods

2.1. Sample preparation

To investigate optical breakdown of hBN monolayers, an optically robust substrate is needed, which disqualifies the popular 90 nm SiO_2-Si substrates [8]. In this work, we used fused silica, whose reported bandgap energy ranges between 7 and 9 eV, which is comparable to 7.7 ± 0.5 eV of hBN monolayers. Al_2O_3 is also disqualified here as it has a Raman peak at 1356 cm^{-1} that overlaps with that of the hBN monolayers (see section S1). The hBN monolayers were grown on 500 nm-thick Cu(111) on c-plan Al_2O_3 substrates by hot-wall CVD using ammonia borane (97%) as the precursor. The as-grown monolayer hBN film was detached from the Cu(111)/Al_2O_3 substrate by electrochemical delamination using a poly(methyl methacrylate) (PMMA) film and a thermal release tape (TRT) as the supporting layer. After detachment, the TRT/PMMA/hBN stacked film was placed on a fused silica substrate. The TRT and PMMA film were finally removed by baking and hot acetone, leaving behind a monolayer hBN film on fused silica. PMMA residue was further removed using rapid thermal annealing at 400 °C for 1 min under a 6 torr forming gas (5% H_2 and 95% nitrogen). Further details of the growth and transfer can be found in [17].

2.2. Laser ablation and patterning setup

The laser employed in this experiment is a Coherent RegA 9000, producing 800 nm 160 fs pulses with a pulse energy stability of ∼0.5%. A circular ND filter wheel was used to control the pulse energy. For single-pulse experiments, the laser was operated at 300 Hz and a fixed number of pulses (between 1 and 10 k pulses) were selected using a mechanical shutter. The laser pulses were focused through a 0.26-NA Mitutoyo NIR microscopy objective (unless otherwise specified) onto the front sample surface. An Aerotech translational stage (ANT-50L, encoder resolution 10 nm, straightness/flatness ± 2 μm) was used for positioning the sample at the laser focus and for moving it between shots. For line scanning experiments, the laser was operated at 100 kHz and focused through a 0.9-NA Leitz objective. The sample was translated at 100 μm s^{-1} using a Newport 9063-XYZ translational stage (straightness/flatness $\pm$ 2 μm) equipped with a New Focus 8310 actuator (encoder resolution = 55 nm) for focus control and two Newport 850-F actuators (encoder resolution = 50 nm) for lateral positioning.

2.3. Imaging

The ablated features were imaged using several modalities. For low-resolution imaging, an optical microscope (Olympus BX-51) in differential interference contrast (DIC) mode was employed. For high-resolution imaging, a field-emission scanning electron microscope (Raith 150) was used with an acceleration voltage between 1 and 5 kV to avoid charging (samples were not metallized). To confirm the monolayer is removed, an atomic force microscope (Veeco Nanoscope IIIa) operated in tapping mode with a tip diameter of 10 nm was used. The open-source software Gwyddion was used for atomic force microscopy (AFM) image processing. For graphene and MoS_2, the ablated features were imaged optically in bright-field mode. Practically, DIC is the simplest method but the contrast sometimes can be an issue. Scanning electron microscopy (SEM) provides high resolution images if substrate charging can be mitigated. AFM provides the highest depth resolution but is slow and suffers PMMA residues remaining from the transfer process.

2.4. Raman, photoluminescence (PL), and UV–vis-NIR absorption spectroscopy

For material analysis, Raman and PL spectra were collected using a home-built epi-luminescent microscope with a 0.9-NA (Olympus 100×) objective. A dichroic filter (Long pass 532 nm, Iridian ZX827) was used to separate the 532 nm continuous-wave excitation (Lasos GLK 3250 T01) from the Raman/PL signal. The signal was then coupled into a 200 μm fiber and detected using an imaging spectrometer (Horiba iHR-550) with a liquid nitrogen cooled charge-coupled device (CCD, Symphony). In the literature, the vast majority of Raman studies of hBN monolayers were conducted on 90 nm SiO_2/Si substrates, where the etalon effect enhanced the signal strength [13]. On transparent substrates which lack the etalon enhancement, the Raman signal strength is extremely weak, which prompted us to use a high laser power (∼5 mW) and long integration time (∼20 min). To further increase the signal-to-noise ratio, a larger focused beam radius ($\omega_o = 1.16$ μm) was used, which compromises the spatial resolution. The UV–vis-NIR absorbance spectrum was collected using a Shimadzu UV2600 spectrophotometer with the hBN monolayer in the sample arm and a blank fused silica substrate in the reference arm.

2.5. Fidelity analysis of ablated features

To quantify the fidelity of laser ablation, i.e. the how well the ablated shape matches the focused laser beam shape, we calculate the percentage area mismatch between the ablated features and the scaled focused laser beam profile. The former was imaged via either OM or AFM, while the latter was imaged using a 0.8 NA 100× objective and a CCD (WinCamD UCD23). For the fidelity analysis, the laser beam profile was scaled to match the ablated features, from which the area difference (in terms of pixel counts) between these two were computed. The above difference was normalized to the ablated area yielding the percentage area mismatch. For more details, refer to section S2.

3. Results and discussion

3.1. Breakdown threshold and reproducibility

Figure 1(a) shows SEM, DIC and AFM images of an array of holes in a hBN monolayer on fused silica ablated with incident pulse energies of 620, 560, 508, 448 and 409 nJ (from top to bottom). The scaling of the hole size with the pulse energy is evident and consistent across different imaging modalities. These pulse energies were converted to the peak internal fluences (in J cm^{-2}) following $F = 200 \cdot \eta^2 E/\pi\omega_o^2$, where $\eta = 0.66$ is the field enhancement factor due to the etalon effect [13], E is the incident pulse energy (in nJ), and ω_o is the focused Gaussian beam waist (in μm). Figure 1(b) displays the hole area A as a function of the peak internal fluence F for three modalities. The data were fitted to Liu's equation $A = (\pi/2)\omega_o^2 \ln(F/F_{th})$ to extract the breakdown threshold fluences F_{th} [18], which are 0.69, 0.71, 0.71 J cm^{-2} for DIC, SEM, AFM modalities, respectively, yielding an average value of 0.70 ± 0.01 J cm^{-2}. This number is the largest among all 2D materials, which is 8× (10×) higher than that of WS_2 (MoS_2) monolayers [19]. Substrate damage was observed for $F \geqslant 1.5 F_{th}$ (or 1.1 J cm^{-2}), evident as a central darker spot in AFM and a brighter spot in DIC images.

To assess the reproducibility of the breakdown thresholds, the above procedure was repeated across the same sample on different days. Figure 1(c) shows the statistics of the retrieved F_{th} based on DIC. Experiments #2 and #4 have multiple runs on the same day on remotely separated locations in the sample, which has a spread of 4% and 2%, respectively. Over different days, the spread can be as large as 14% (or ±7%). This number is on par with the 10% reproducibility reported for nanosecond-picosecond laser ablation [20]. The reproducibility of F_{th} is influenced by many factors. The small spread of F_{th} in experiments #2 and 4 indicates the sample is quite uniform across the substrate in terms of film quality (e.g. defect density, strain field, etc), PMMA residue, and substrate imperfection (e.g. roughness, cracks, grooves, pores, etc). These set the lower limit of the reproducibility. The remaining spread is most likely due to the irreproducibility of laboratory conditions such as laser beam quality (e.g. beam size, pulse width, chirp, etc) and the humidity and temperature of the room.

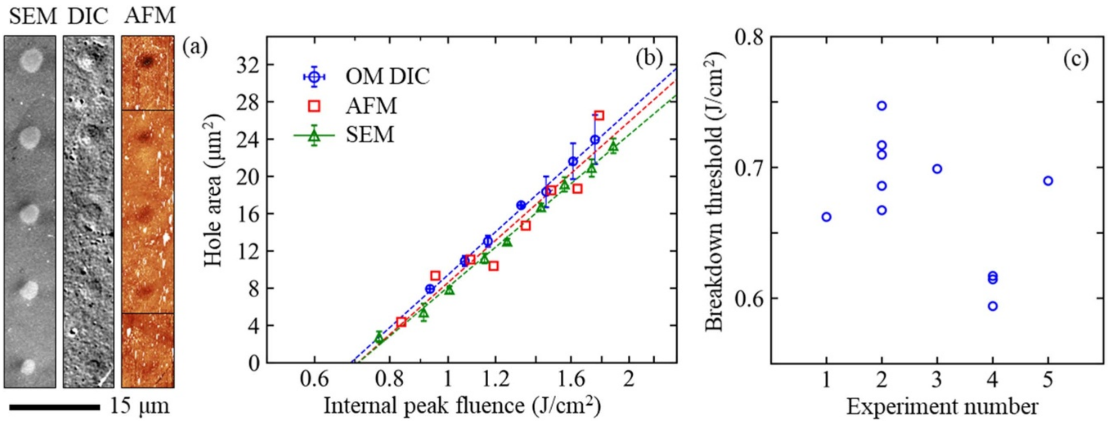

Figure 1. (a) SEM, DIC and AFM images of the same ablated features in a hBN monolayer on fused silica, produced with a laser beam radius of ∼4 μm and with decreasing pulse energy from top to bottom. The scale bars are 15 μm. (b) A linear-log plot of ablated hole area vs. internal peak fluence for three imaging modalities. (c) Reproducibility of breakdown thresholds on the same sample over different days and geographic locations across the sample.

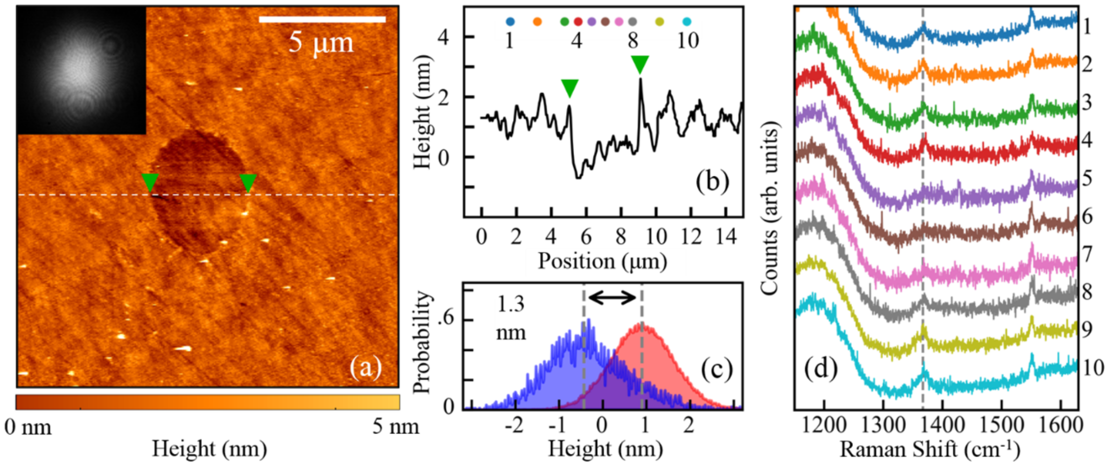

Figure 2. (a) Ablated hole in hBN on fused silica with an internal peak fluence of 0.86 J cm^{-2}. The focused laser beam radii (1/e^2-intensity) is 6.32 μm. The white particles of varying shapes and sizes are PMMA residue from the transfer process. The inset shows the laser beam image captured via CCD. (b) Cross-sectional line profile of a 1.2 nm thick stripe of (a) represented by the dotted line. Green arrows indicate the edge of the hole. (c) Histogram of height data of (a) inside the hole (blue data) and region outside the hole (red data). (d) Raman signals collected across (a). The signals correspond to colored markers in (b).

3.2. Evidence of clean removal

Figure 2(a) shows an ablated hole in hBN obtained with an internal peak fluence of 0.86 J cm^{-2} ($F = 1.27 F_{th}$), whose cross-sectional height profile (averaged over a horizontal strip of 1.2 nm wide) along the dashed line is displayed in figure 2(b) with green arrows indicating the edges of the hole. Figure 2(c) shows histograms of AFM height data within the hole (blue trace) and of the pristine film (red trace). The blue trace appears noisier than the red because of fewer pixels for statistical averaging. The difference in the peak positions indicates a film height of ∼1.3 nm, which is consistent with the literature value of 0.3–2.8 nm for hBN monolayers [1, 8]. The width of the histogram for the hole is 1.95 nm, which is slightly larger than 1.76 nm of the pristine film, suggesting that the hBN film acts like a carpet to hide the surface roughness of the underlying bare substrate. The surface roughness inside the hole (figure 2(c)) is the same as that of the bare substrate (see section S3), indicating the monolayer is removed without damaging the substrate at this fluence.

Figure 2(d) displays Raman spectra taken across the hole in figure 2(a), with each spectrum displaced vertically for clarity. The color-coded circles in figure 2(b) mark the positions where the Raman signals were collected. The common features of a broad peak at ∼1185 cm^{-1} and a smaller one at 1553 cm^{-1} are attributed to the fused silica substrate (see section S1). The E$_{2g}$ in-plane optical phonon Raman peak at 1367 cm^{-1} is weak yet clearly resolved and consistent with literature values of 1366–1370 cm^{-1} for hBN monolayers [1, 21]. This peak vanishes within the hole (traces #5-7), indicating a clean removal of the film by the ablation process. The Raman spectra near the border of the hole (traces # 3, 4, 8, 9)

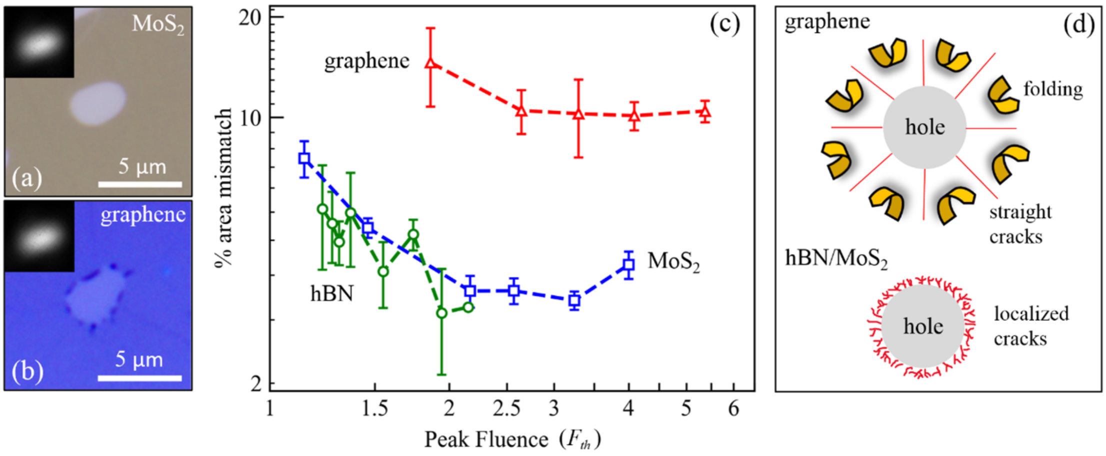

Figure 3. (a) An ablated hole in MoS$_2$ monolayer flakes displaying smooth edges, and (b) an ablated hole in graphene monolayer film displaying folding around the edges. Both results were performed on 90 nm SiO$_2$-Si substrates [13] with a laser beam waist of 2.2 μm. The insets show the laser beam images captured via CCD. (c) Calculated percentage area mismatch vs internal peak fluence (in units of F_{th}) data for hBN, MoS$_2$, and graphene. (d) Illustration (not to scale) of different crack propagation in hBN (MoS$_2$) and graphene.

show no new peaks or frequency shifts of existing peaks within our detection limit. The absence of new peaks is in sharp contrast to a previous report [8], in which a new Raman peak at 1295 cm^{-1} corresponding to cubic boron nitride (cBN) nano-crystals was observed when the ablation was incurred by 80 MHz nano-joule femtosecond pulses. Frequency shifts, if they exist, would indicate the presence of strains originating from vacancies and lattice disorder introduced by the ablation, which was observed in MoS$_2$ monolayers [19]. The lack of such changes reveals that hBN monolayers remain pristine around the edge of the ablated hole, even at an intensity close to the breakdown threshold.

3.3. Patterning fidelity

Figure 2(a) reveals that the circumference of the ablated hole matches the laser beam shape. A similar result was obtained for MoS$_2$ monolayer (figure 3(a)). This is in stark contrast to graphene, which exhibits petal-like folds outwards away from the ablated hole (figure 3(b) or [22] for a demonstration with a stronger contrast). Graphene folding was found universally on supporting substrates, possibly due to the rapid substrate expansion during the laser heating [22], which makes high-fidelity patterning of graphene difficult using femtosecond ablation [23]. To quantify the fidelity, the percentage area mismatch is calculated (see section S2) and plotted as a function of the internal peak fluence (in units of F_{th}) for graphene, MoS$_2$, and hBN (figure 3(c)). As shown, the percentage area mismatch is comparable for hBN and MoS$_2$ monolayers but is 4× smaller than that of graphene. We attribute this sharp contrast in fidelity to their different fracture toughness, which is the ability of a material to resist catastrophic fracture [24, 25]. Take graphene and hBN as examples. The removal of atoms in the film via laser ablation introduces compressive stress on the edge of the film [26] and cracks initiate from stress concentration sites. For graphene, the cleavage of the bonds results in two identical zigzag edges. Because of this symmetric edge stress, the crack tip propagates along a straight line over a longer distance (i.e. low fracture toughness) [27]. Upon the fast substrate expansion induced by the laser heating, the remaining graphene between two adjacent cracks fold [22], leading to the higher area mismatch and lower fidelity (figure 3(d)). For hBN, the situation is entirely different [25]. The cleavage of h-BN bonds results in two different types of zigzag edge: a B-terminated edge (B-edge) and an N-terminated edge (N-edge), of which the B-edge has twice the edge stress than that of the N-edge [25]. Because of this asymmetric edge stress, the crack tip bifurcates first and then deflects from its original propagation direction, and consequently the B-edge and N-edge swap their positions relative to the crack tip owing to their three-fold symmetry [25]. Cracks propagate via repeated deflection and sometimes branch, dissipating substantial energy to form a high density of localized damage close to the edge of the hole (i.e., high fracture toughness). Experiments have shown hBN has a fracture toughness up to 10× higher than graphene [25, 27]. The same fracture physics can be applied to other heterogeneous 2D crystals with three fold symmetry such as MoS$_2$ [25], which is supported by our data in figure 3(c). Our result indicates femtosecond laser patterning of hBN and MoS$_2$ has high fidelity and can generate deterministic features.

3.4. Role of defects in optical breakdown

Figure 4(a) compares the surface breakdown threshold of PMMA (2.0 J cm^{-2}) and Al$_2$O$_3$ (4.7 J cm^{-2}) (see section S4) and the breakdown threshold of hBN (0.7 J cm^{-2}). For the purpose of

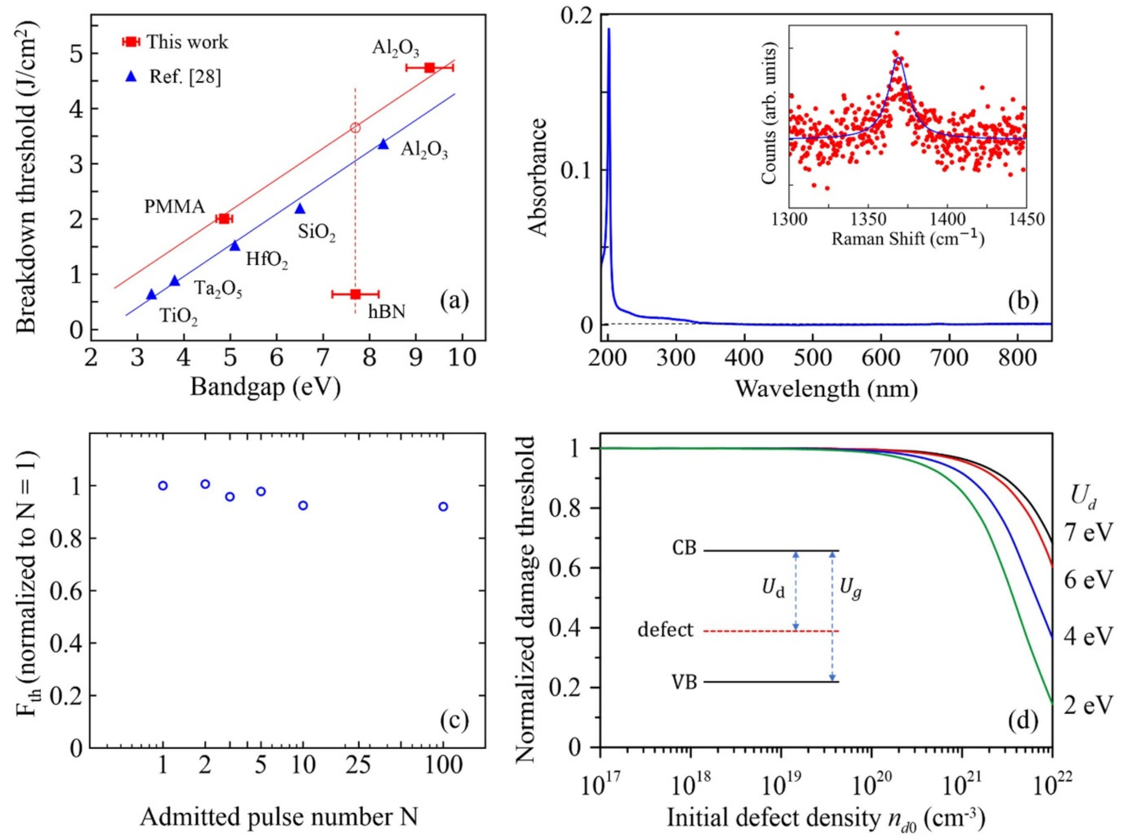

Figure 4. (a) Breakdown threshold vs. bandgap (see section S4) for hBN monolayer, Al_2O_3, and PMMA, obtained in this work. Also included are data (red triangles) from [28] for comparison. (b) UV–vis-NIR absorbance and Raman (as inset, with substrate spectrum subtracted) spectra of hBN monolayer on fused silica. (c) Multi-pulse breakdown threshold fluence vs. admitted pulse number. (d) Normalized damage/breakdown threshold vs. initial defect density for selected defect bandgap energies. The inset shows a schematic energy diagram.

discussion, it also displays breakdown threshold of various amorphous thin films from [28]., measured with a similar pulse width as ours. Their data, along with other reports [29, 30], shows F_{th} scales linearly with bandgap energy. If we apply this linear scaling to our PMMA and Al_2O_3, the red empty circle is the interpolated $F_{th} \sim 3.8$ J cm^{-2} for a fictitious bulk dielectric with a bandgap energy of 7.7 eV, which is 5.4 times larger than our reported F_{th} of the monolayer hBN. Physical imperfection on the surface, such as sub-wavelength cracks, grooves, and voids, were reported to lower breakdown threshold of bulk dielectrics by a factor of 2–5 via electric field enhancement [20]. This is likely not the case here, as all our ablated holes are at the geometric center of the laser beam and their shapes resemble the beam, even though very fine surface scratches are present within the hole (see the upper right corner of the hole in figure 2(a)).

Atomic defects are also known to lower the breakdown threshold of bulk dielectrics. Defects could do so mechanically by weakening bonds to destabilize the lattice and by building up tensile pressure, which was the proposed cause for a factor of 4 reduction in extreme ultraviolet (XUV) ablation threshold of LiF by molecular dynamic simulation [31]. Defects could also do so electronically by seeding electrons to the conduction band. It is generally accepted that optical breakdown is initiated by seed carriers followed by avalanche ionization [20]. In the absence of defects, such seed electrons are generated from photoionization of valence electrons. In the presence of defects, however, they can be background carriers from shallow donors or derived from photoionization of occupied intragap defect states. The latter possibility was examined by Hellwarth, who showed a deep-lying impurity density of 10^{18} cm^{-3} is required to lower breakdown threshold of polar crystals [20]. With this in mind, we characterized defects in our samples using various optical spectroscopies. PL spectra excited by 532 nm show no distinction between hBN monolayer on fused silica and bare fused silica (see section S5), revealing the absence of vis-NIR radiative defects. The UV–vis-NIR absorbance spectrum (figure 4(b)) shows a narrow exciton absorption band around 201 nm and an absorption tail in the range of 215–400 nm (3.1–5.7 eV). Similar absorption spectra from CVD-grown hBN were reported earlier that were attributed to optical transitions associated with common defects in hBN, including substitutional carbon impurity on nitrogen sublattice (C_N), the boron vacancy (V_B), the nitrogen vacancy (V_N), and the boron-nitrogen vacancy (V_{BN}) [32, 33]. Our Raman spectrum displays a peak wavelength of 1367 cm^{-1} and a FWHM linewidth of 20 cm^{-1} (see the inset in figure 4(b)). The peak position is red-shifted with respect to that of exfoliated monolayer supported on substrates ($\sim$1369 cm^{-1}), which we attribute to tensile strains originating from these atomic defects [21, 34]. The Raman linewidth is larger than that of exfoliated monolayer on substrates ($\sim$10–13 cm^{-1}), which we attribute to inhomogeneously distributed strain fields within the micrometer-sized laser spot, as the monolayer follows the substrate's roughness [34]. As for the defect density, transport studies have reported a trap density anywhere between $10^{12}-10^{17}\,\mathrm{cm}^{-3}$ for exfoliated hBN [35, 36]. Given the defect density can be 2–3 orders higher for CVD hBN [36], this amounts to a maximum bulk defect density of $10^{19}-10^{20}\,\mathrm{cm}^{-3}$, corresponding to a surface density of $10^{12}-10^{13}\,\mathrm{cm}^{-2}$ for monolayer hBN and a mean separation of 3–10 nm between defects. It is evident that there are abundant defects interacting with the laser pulse. If these defects were to lower the breakdown threshold, either mechanically or electronically, then adding more defects should reduce it further. To verify this hypothesis, we measured the multi-pulse breakdown threshold $F_{th}(N)$ of our hBN monolayer as a function of admitted pulse number N [19]. The data is displayed in figure 4(c), revealing a very weak dependence of breakdown threshold on the admitted pulse number: $F_{th}(N)$ drops only by less than 10% for 10 pulses compared to the single pulse. According to the theory of incubation [37], as $F_{th}(N)$ is only slightly smaller than $F_{th}(1)$, the first $N-1$ pulses in the N pulse train will surely add defects and yet the N^{th} pulse needs a fluence comparable to $F_{th}(1)$ to induce breakdown. This means all the defects created by the leading $N-1$ pulses do very little to lower the breakdown threshold. This disapproves the above hypothesis.

The conclusion is also supported by the numerical modeling presented below. For simplicity, we consider a bulk dielectric with pre-existing background carrier density n_{e0} and one intragap defect state with an initial density n_{d0} (see the inset of figure 4(d)). Denoting the carrier density in the conduction band as n_e, the initial valance band electron density as n_{v0}, the intragap defect density as n_d, and the atomic density as n_a, the transient population evolution for n_e and n_d including saturation can be described by the following simple rate equation [38]:

$$\begin{aligned}\frac{dn_e}{dt} &= \left[W_{PI}(U_g)+W_{AI}(U_g)\,n_e\right]\left(1-\frac{n_e}{n_{v0}}\right)\\ &\quad+\left[W_{PI}(U_d)+W_{AI}(U_d)\,n_e\right]\left(\frac{n_d}{n_a}\right)-\frac{n_e}{\tau_c},\\ \frac{dn_d}{dt} &= \frac{n_e}{\tau_{cd}}-\left[W_{PI}(U_d)+W_{AI}(U_d)\,n_e\right]\left(\frac{n_d}{n_a}\right)\end{aligned}\qquad(1)$$

where U_g and U_d are respectively the bandgap energies of the valence band and the intragap defect, τ_c is the carrier lifetime, and τ_{cd} is the carrier relaxation time from the conduction band to the defect state. In equation (1), $W_{PI}(U)$ is the photoionization rate per unit volume and $W_{AI}(U)$ is the avalanche ionization rate per conduction electron, for a transition across a bandgap energy U. For the purpose of calculation, we adopt Keldysh's formula [39] for the former and an avalanche model based on laser plasma heating for the latter [40]. As this simple rate equation is known to overestimate AI [41], we employ a fudge factor γ to slow it down. The total n_e at the end of the pulse is obtained by integrating equation (1) numerically using n_{e0}, n_{d0} and U_d as independent parameters (see section S6 for details including simulation parameters). Breakdown threshold fluence F_{th} is defined when the peak total n_e at the center of the pulse equals 5% of the valence electron density [42]. For this fictitious bulk dielectric, $\gamma_{3D}\sim0.085$ is determined by fitting equation (1) to F_{th} of 3.8 J cm^{-2}, assuming no defects are present.

The pre-existing background carrier concentration n_{e0} in our sample can be estimated as follows. Using a similar growth technique as ours, Chen *et al* reported a resistivity of 529 Ωcm for monolayer hBN flakes [43]. Assuming an electron mobility of 35 $\mathrm{cm}^2\,(\mathrm{V}\cdot\mathrm{s})^{-1}$ [44], this translates to a background carrier density of $n_{e0}\sim10^{8}\,\mathrm{cm}^{-3}$. Numerically, we found this initial condition has no influence on total n_e. This can be understood as follows. Stuart *et al* has shown that, assuming a temporally flat pulse, equation (1) can be simplified to define an effective photoionized carrier density as $W_{PI}(U_g)/W_{AI}(U_g)$ [45]. This number is estimated to be $\sim3.3\times10^{21}\,\mathrm{cm}^{-3}$ at the breakdown threshold of this fictitious material (see section S6 for details), which is 13 orders of magnitude lager than n_{e0}. We conclude that background carriers from shallow donors have no effect on F_{th}. On the other hand, the bandgap U_d of these intragap defect states in hBN can be estimated from density functional theory. Wirtz *et al* showed that C_N, V_B, and V_{BN} have occupied states very close to the valence band with $U_d\leqslant7\,eV$, while V_N has an occupied mid-gap state with $U_d\approx4.1$ eV from the conduction band edge. Figure 4(d) displays calculated F_{th}, normalized to the intrinsic threshold of 3.8 J cm^{-2}, as a function of initial defect density n_{d0} for selected defect bandgap energies U_d. As shown, even for the worst case of $n_{d0}=10^{20}\,\mathrm{cm}^{-3}$, the breakdown threshold stays nearly the same for $4\leqslant U_d\leqslant7\,eV$. We conclude that intragap defect states have a negligible effect on F_{th} either. We note that, even though the choices of $W_{PI}(U)$ and a 5% critical carrier density for breakdown are somewhat arbitrary, the conclusion drawn from this analysis is robust against variation in these parameters (see section S6 for details).

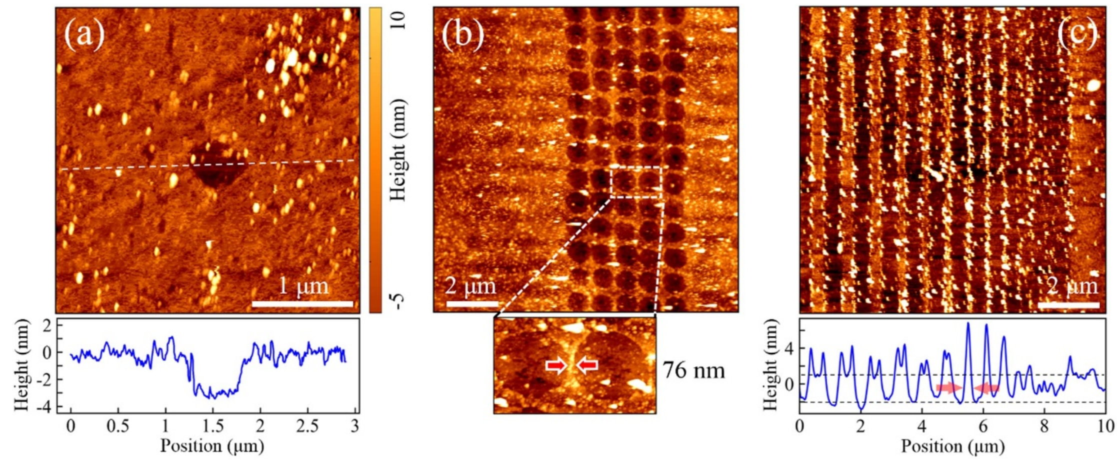

Figure 5. AFM images of patterned hBN using femtosecond laser: (a) an isolated hole, (b) an array of holes, and (c) an array of line cuts with decreasing hatching distance. The bottoms of (a) and (c) are a cross-sectional AFM height profile and column-averaged cross-sectional AFM height profile, respectively, and the bottom of (b) is the zoomed-in of the dashed box. See text for details.

3.5. Enhanced carrier generation in hBN monolayers

Our multi-pulse threshold experiment (figure 4(c)) and modeling (figure 4(d)) show that defects alone cannot explain the 4–5× reduction in F_{th} of hBN monolayers compared to their bulk equivalent. We conclude this reduction is intrinsic, i.e. carrier generation in hBN monolayer is more efficient. For example, assuming $W_{PI}(U)$ is the same for 2D and 3D dielectrics and fitting equation (1) to F_{th} of hBN monolayer $\sim$0.7 J cm^{-2}, we obtain $\gamma_{2D} \sim 2$, which is 24× larger than $\gamma_{3D} \sim 0.085$. In reality, both photoionization and avalanche ionization in hBN could be enhanced. Enhanced 2–3 multiphoton interband transitions in monolayer MoS_2 was reported earlier [46–48]. For hBN, Ji *et al* has reported enhanced 2-photon absorption to exciton states at wavelength $\lambda = 400$ nm and enhanced 3-photon absorption to the defect states at $\lambda = 600$–800 nm in a 5-layered hBN [33]. Such processes could possibly contribute to an enhanced interband transition, albeit it can be challenging to detect. In contrast to multiphoton absorption, there is no literature report on avalanche ionization in 2D materials, although its reverse process—Auger recombination—has been studied. Auger recombination rates in transition metal dichalcogenide monolayers were shown 10–10^6× larger than bulk materials due to enhanced Coulomb interaction among electrons [49, 50]. These findings imply avalanche ionization may possibly be enhanced in 2D materials as well.

The above finding has strong implications for future work involving strong-field interaction with 2D materials. As substrates are practically necessary to support 2D materials, it is intuitive to use a substrate with a large bandgap to avoid optical damage. The data in figure 4(a) eliminates this constraint and enables the use of lower-bandgap materials with additional desired merits. For example, diamond has a lower bandgap ($\sim$5.5 eV) and 10× better thermal conductivity than hBN. In the quest for high harmonic generation in hBN, it may thus be advantageous to use diamond substrates to dissipate heat efficiently and avoid thermal damage under repetitive high intensity excitation. As another example, Stemme *et al* have demonstrated high-speed (50 mm s^{-1}) and high-spatial-resolution (100 nm) patterning of $PtSe_2$, MoS_2, and graphene using a commercial femtosecond two-photon 3D printer [14]. Low-cost borosilicate glass wafers with a bandgap energy of 3–4 eV can serve as the supporting substrates for large-scale laser pattering of hBN instead of more expensive Al_2O_3 or fused silica.

3.6. Sub-micron resolution patterning

By using a 0.9-NA objective and a fluence close to the breakdown threshold ($F = 1.1F_{th}$), figure 5(a) shows an AFM image of a hole with a diameter of $\sim$500 nm in hBN. This sets the resolution of the material removal (i.e. the minimum hole diameter or the line cut width). Figure 5(b) shows an array of holes ablated with a fluence of $1.75F_{th}$ and a 0.55-NA objective. The periodicity is 1 μm and the average diameter of the holes is 830 nm. The zoomed-in AFM image (bottom) shows left-over film width of $\sim$76 nm between two adjacent holes. Figure 5(c) shows an AFM image of an array of line cuts obtained with a fluence of $\sim 1.5F_{th}$ and a 100 μm s^{-1} scanning speed, rendering a line cut width of 330 nm. The bottom plot displays a column-averaged cross-sectional height profile obtained by stacking all columns and then dividing it by the number of columns to remove low-frequency spatial noise. The hatching distance starts at 1 μm and decreases by 50 nm per line, leading to a gradual decrease of the strip width. The PMMA residue is more pronounced in this region of the sample, especially along the edges of the stripes, which suggests these PMMA particles may have aggregated upon laser irradiation. These aggregates lead to the fork-like features in the height profile, which evolve into peaks for very small hatching distance of the laser beam. The stripes display width variation and edge roughness due to the finite positioning stability of the translation stage in the depth and lateral directions, which was hampered by the cross coupling from the moving vertical axis. The horizontal dashed lines delineate the top and bottom of the film, from which the narrower stripe width is determined to be ∼240 nm. When the hatching distance is too small, hBN stripes become partially removed due to the positioning instability. Holes and line cuts demonstrated in figure 5 form the basic building blocks for more sophisticated structures and have plenty of room for improvement: Ablation resolution can be improved by using a shorter wavelength, narrower strip width can be obtained by a more stable translational stage or employing beam shaping techniques [12], and higher throughout can be obtained using a galvo scanner [14]. Moreover, a more effective recipe for cleaning PMMA residue [9] or a residue-free transferring agent such as PDMS [51] can be adopted to improve surface cleanness.

4. Conclusions

In conclusion, we report the first systematic study of dielectric breakdown of CVD-grown hBN monolayers induced by single femtosecond laser pulses. With its highest quasiparticle bandgap energy, hBN monolayers was found to have the largest intrinsic breakdown threshold fluence of 0.7 J cm^{-2}, which is 7–8× higher than that of WS_2 and MoS_2 monolayers. Raman spectra indicated hBN was completely removed within the ablated hole and remained pristine in the surrounding of the hole, while AFM revealed substrate stayed intact for $F \leqslant 1.5F_{th}$. In addition, optical and atomic force microscopies reveal that the ablation features exhibit excellent fidelity with very small edge roughness, which we attribute to its ultrahigh fracture toughness as a result of its heterogeneous nature with three-fold symmetry. Moreover, even though defects are known to be abundant in CVD-grown hBN, its multi-pulse breakdown threshold was found only marginally lower than that of the single pulse, indicating nonlinear optical breakdown in hBN is intrinsic, i.e. not affected by defects. This conclusion is supported by numerical modeling based on simple coupled rate equations incorporating defects. Furthermore, we found hBN monolayers have a 4–5× lower breakdown threshold than their bulk counterpart with the same bandgap energy. As defects cannot be responsible for such a reduction, such a reduction can only be understood if the carrier generation in monolayers is enhanced due to its 2D nature. Specifically, our theory reveals a maximum 24× enhancement of avalanche ionization efficiency is possible. This finding enables low-cost substrates with a smaller bandgap to support hBN for wafer-scale laser patterning. Finally, we demonstrate laser patterning of array of holes and lines in hBN with sub-wavelength feature sizes, which serve as basic building blocks for more sophisticated patterns. We consider that the findings presented in this work could advance the understanding of the fundamental properties of monolayer h-BN, especially in the optical breakdown limit. Moreover, our work firmly establishes the femtosecond laser as a novel and promising tool for one-step resist-free patterning of hBN monolayers with high fidelity.

Data availability statement

All data that support the findings of this study are included within the article (and any supplementary files).

Acknowledgments

We greatly appreciate the following people: Dr Jimmie A Miller (UNCC) for assistance in AFM measurements, Professor Stuart T Smith (UNCC) for discussions on fracture toughness, Professor Haitao Zhang and Mr Simon M Sami (UNCC) for use of their Shimadzu spectrophotometer, Mr Shih-Chu Lin for sample preparation, Mr Yang-Jiang Li (NYCU) for absorption measurement, and Mr Kenan Darden (UNCC) for proofreading. W-H C acknowledges the support from the National Science and Technology Council of Taiwan (NSTC 111-2119-M-A49-005-MBK).

ORCID iDs

Sabeeh Irfan Ahmad https://orcid.org/0009-0002-6287-7206
Arpit Dave https://orcid.org/0009-0003-1527-2615
Emmanuel Sarpong https://orcid.org/0000-0002-3483-3081
Tsing-Hua Her https://orcid.org/0000-0003-1360-9942

References

[1] Li L H and Chen Y 2016 Atomically thin boron nitride: unique properties and applications *Adv. Funct. Mater.* **26** 2594–608

[2] Caldwell J D, Aharonovich I, Cassabois G, Edgar J H, Gil B and Basov D N 2019 Photonics with hexagonal boron nitride *Nat. Rev. Mater.* **4** 552–67

[3] Henriques J C G, Ventura G B, Fernandes C D M and Peres N M R 2020 Optical absorption of single-layer hexagonal boron nitride in the ultraviolet *J. Phys.: Condens. Matter* **32** 025304

[4] Li Y, Rao Y, Mak K F, You Y, Wang S, Dean C R and Heinz T F 2013 Probing symmetry properties of few-layer MoS_2 and h-BN by optical second-harmonic generation *Nano Lett.* **13** 3329–33

[5] Popkova A A, Antropov I M, Fröch J E, Kim S, Aharonovich I, Bessonov V O, Solntsev A S and Fedyanin A A 2021 Optical third-harmonic generation in hexagonal boron nitride thin films *ACS Photonics* **8** 824–31

[6] Le Breton G, Rubio A and Tancogne-Dejean N 2018 High-harmonic generation from few-layer hexagonal boron nitride: evolution from monolayer to bulk response *Phys. Rev.* B **98** 165308

[7] Gao X, Pandey S, Kianinia M, Ahn J, Ju P, Aharonovich I, Shivaram N and Li T 2021 Femtosecond laser writing of spin defects in hexagonal boron nitride *ACS Photonics* **8** 994–1000

[8] Hou S, Birowosuto M D, Umar S, Anicet M A, Tay R Y, Coquet P, Tay B K, Wang H and Teo E H T 2018 Localized emission from laser-irradiated defects in 2D hexagonal boron nitride *2D Mater.* **5** 015010

[9] Garcia A G F, Neumann M, Amet F, Williams J R, Watanabe K, Taniguchi T and Goldhaber-Gordon D 2012 Effective cleaning of hexagonal boron nitride for graphene devices *Nano Lett.* **12** 4449–54

[10] Elbadawi C *et al* 2016 Electron beam directed etching of hexagonal boron nitride *Nanoscale* **8** 16182–6

[11] Martin A A, McCredie G and Toth M 2015 Electron beam induced etching of carbon *Appl. Phys. Lett.* **107** 041603

[12] Stöhr R J, Kolesov R, Xia K and Wrachtrup J 2011 All-optical high-resolution nanopatterning and 3D suspending of graphene *ACS Nano* **5** 5141–50

[13] Solomon J M, Ahmad S I, Dave A, Lu L-S, HadavandMirzaee F, Lin S-C, Chen S-H, Luo C-W, Chang W-H and Her T-H 2022 Ultrafast laser ablation, intrinsic threshold, and nanopatterning of monolayer molybdenum disulfide *Sci. Rep.* **12** 6910

[14] Enrico A, Hartwig O, Dominik N, Quellmalz A, Gylfason K B, Duesberg G S, Niklaus F and Stemme G 2023 Ultrafast and resist-free nanopatterning of 2D materials by femtosecond laser irradiation *ACS Nano* **17** 8041–52

[15] Li P, Dolado I, Alfaro-Mozaz F J, Casanova F, Hueso L E, Liu S, Edgar J H, Nikitin A Y, Vélez S and Hillenbrand R 2018 Infrared hyperbolic metasurface based on nanostructured van der Waals materials *Science* **359** 892–6

[16] Fröch J E, Hwang Y, Kim S, Aharonovich I and Toth M 2019 Photonic nanostructures from hexagonal boron nitride *Adv. Opt. Mater.* **7** 1801344

[17] Chen T-A *et al* 2020 Wafer-scale single-crystal hexagonal boron nitride monolayers on Cu (111) *Nature* **579** 219–23

[18] Liu J M 1982 Simple technique for measurements of pulsed Gaussian-beam spot sizes *Opt. Lett.* **7** 196–8

[19] Solomon J M, Ahmad S I, Dave A, Lu L-S, Wu Y-C, Chang W-H, Luo C-W and Her T-H 2022 Ultrafast multi-shot ablation and defect generation in monolayer transition metal dichalcogenides *AIP Adv.* **12** 015217

[20] Bloembergen N 1974 Laser-induced electric breakdown in solids *IEEE J. Quantum. Electron.* **10** 375–86

[21] Cai Q, Scullion D, Falin A, Watanabe K, Taniguchi T, Chen Y, Santos E J G and Li L H 2017 Raman signature and phonon dispersion of atomically thin boron nitride *Nanoscale* **9** 3059–67

[22] Yoo J-H, In J B, Park J B, Jeon H and Grigoropoulos C P 2012 Graphene folds by femtosecond laser ablation *Appl. Phys. Lett.* **100** 233124

[23] Sahin R, Simsek E and Akturk S 2014 Nanoscale patterning of graphene through femtosecond laser ablation *Appl. Phys. Lett.* **104** 053118

[24] Stephens R I 2000 *Metal Fatigue in Engineering* (Wiley)

[25] Yang Y *et al* 2021 Intrinsic toughening and stable crack propagation in hexagonal boron nitride *Nature* **594** 57–61

[26] Deng J, Fampiou I, Liu J Z, Ramasubramaniam A and Medhekar N V 2012 Edge stresses of non-stoichiometric edges in two-dimensional crystals *Appl. Phys. Lett.* **100** 251906

[27] Zhang P *et al* 2014 Fracture toughness of graphene *Nat. Commun.* **5** 3782

[28] Mero M, Liu J, Rudolph W, Ristau D and Starke K 2005 Scaling laws of femtosecond laser pulse induced breakdown in oxide films *Phys. Rev.* B **71** 115109

[29] Joglekar A P, Liu H H, Meyhofer E, Mourou G and Hunt A J 2004 Optics at critical intensity: applications to nanomorphing *Proc. Natl Acad. Sci. USA* **101** 5856–61

[30] Chris B S, André B and Eric M 2001 Laser-induced breakdown and damage in bulk transparent materials induced by tightly focused femtosecond laser pulses *Meas. Sci. Technol.* **12** 1784

[31] Cherednikov Y, Inogamov N A and Urbassek H M 2013 Influence of defects on extreme ultraviolet laser ablation of LiF *Phys. Rev.* B **88** 134109

[32] Attaccalite C, Bockstedte M, Marini A, Rubio A and Wirtz L 2011 Coupling of excitons and defect states in boron-nitride nanostructures *Phys. Rev.* B **83** 144115

[33] Ouyang Q, Zhang K, Chen W, Zhou F and Ji W 2016 Nonlinear absorption and nonlinear refraction in a chemical vapor deposition-grown, ultrathin hexagonal boron nitride film *Opt. Lett.* **41** 1368–71

[34] Gorbachev R V *et al* 2011 Hunting for monolayer boron nitride: optical and Raman signatures *Small* **7** 465–8

[35] Pierret A *et al* 2022 Dielectric permittivity, conductivity and breakdown field of hexagonal boron nitride *Mater. Res. Express* **9** 065901

[36] Ranjan A *et al* 2023 Molecular bridges link monolayers of hexagonal boron nitride during dielectric breakdown *ACS Appl. Electron. Mater.* **5** 1262–76

[37] Sun Z, Lenzner M and Rudolph W 2015 Generic incubation law for laser damage and ablation thresholds *J. Appl. Phys.* **117** 073102

[38] Chimier B, Utéza O, Sanner N, Sentis M, Itina T, Lassonde P, Légaré F, Vidal F and Kieffer J C 2011 Damage and ablation thresholds of fused-silica in femtosecond regime *Phys. Rev.* B **84** 094104

[39] Keldysh L V 1965 Ionization in field of a strong electromagnetic wave *Sov. Phys.* **20** 1307–14

[40] Sudrie L, Couairon A, Franco M, Lamouroux B, Prade B, Tzortzakis S and Mysyrowicz A 2002 Femtosecond laser-induced damage and filamentary propagation in fused silica *Phys. Rev. Lett.* **89** 186601

[41] Rethfeld B 2004 Unified model for the free-electron avalanche in laser-irradiated dielectrics *Phys. Rev. Lett.* **92** 187401

[42] Sokolowski-Tinten K, Bialkowski J and von der Linde D 1995 Ultrafast laser-induced order-disorder transitions in semiconductors *Phys. Rev.* B **51** 14186–98

[43] Deng S, Gu Y, Wan X, Gao M, Xu S, Chen K and Chen H 2021 Probing electronic properties of CVD monolayer hexagonal boron nitride by an atomic force microscope *Front. Mater. Sci.* **8** 735344

[44] Maity A, Grenadier S J, Li J, Lin J Y and Jiang H X 2021 Hexagonal boron nitride: epitaxial growth and device applications *Prog. Quantum Electron.* **76** 100302

[45] Stuart B C, Feit M D, Herman S, Rubenchik A M, Shore B W and Perry M D 1996 Nanosecond-to-femtosecond laser-induced breakdown in dielectrics *Phys. Rev.* B **53** 1749–61

[46] Zhou F and Ji W 2017 Two-photon absorption and subband photodetection in monolayer MoS_2 *Opt. Lett.* **42** 3113–6

[47] Zhou F and Ji W 2017 Giant three-photon absorption in monolayer MoS_2 and its application in near-infrared photodetection *Laser Photonics Rev.* **11** 1700021

[48] Li Y, Dong N, Zhang S, Zhang X, Feng Y, Wang K, Zhang L and Wang J 2015 Giant two-photon absorption in monolayer MoS_2 *Laser Photonics Rev.* **9** 427–34

[49] Salehzadeh O, Tran N H, Liu X, Shih I and Mi Z 2014 Exciton kinetics, quantum efficiency, and efficiency droop of monolayer MoS_2 light-emitting devices *Nano Lett.* **14** 4125–30

[50] Cunningham P D, McCreary K M and Jonker B T 2016 Auger recombination in chemical vapor deposition-grown monolayer WS_2 *J. Phys. Chem. Lett.* **7** 5242–6

[51] Jain A, Bharadwaj P, Heeg S, Parzefall M, Taniguchi T, Watanabe K and Novotny L 2018 Minimizing residues and strain in 2D materials transferred from PDMS *Nanotechnology* **29** 265203